Ion energy distributions, electron temperatures, and electron densities in Ar, Kr, and Xe pulsed discharges

Hyungjoo Shin, Weiye Zhu, Demetre J. Economou,[a] and Vincent M. Donnelly[b]
Plasma Processing Laboratory, Department of Chemical and Biomolecular Engineering,
University of Houston, 4800 Calhoun Road, Houston, Texas 77204-4004

Ion energy distributions (IEDs) were measured near the edge of Faraday-shielded, inductively coupled pulsed plasmas in Ar, Kr, or Xe gas, while applying a synchronous dc bias on a boundary electrode, late in the afterglow. The magnitudes of the full width at half maximum of the IEDs were $Xe > Kr > Ar$, following the order of the corresponding electron temperatures in the afterglow, $T_e(Xe) > T_e(Kr) > T_e(Ar)$. The measured decays of T_e with time in the afterglow were in excellent agreement with predictions from a global model. Measured time-resolved electron and positive ion densities near the plasma edge did not decay appreciably, even in the 80 μs long afterglow. This was attributed to transport of ions and electrons from the higher density central region of the plasma to the edge region, balancing the loss of plasma due to diffusion. This provides a convenient means of maintaining a relatively constant plasma density in the afterglow during processing using pulsed plasmas. © 2012 American Vacuum Society. [http://dx.doi.org/10.1116/1.4705515]

I. INTRODUCTION

Control of ion energy is critical for maximizing selectivity and minimizing damage in plasma etching for integrated circuit manufacturing. The ion energy distribution (IED) on the substrate electrode is often controlled by applying bias power separately from the source power used for sustaining the plasma. That way, independent (or quasi-independent) control of the IED may be achieved. The IED can be controlled by varying the frequency of the applied rf bias. If the ion transit time (τ_{ion}) through the sheath over the substrate is smaller than the inverse of the bias frequency, $\tau_{ion} < (2\pi f)^{-1}$, a bimodal ion energy distribution is obtained.[1–4] The IED becomes narrower as the applied frequency increases, and the two peaks of the IED eventually overlap at very high frequencies.[5] Instead of a sinusoidal rf bias, a tailored voltage waveform can also be applied to narrow the IED.[6]

As feature sizes shrink to the nanometer scale, narrow IEDs are necessary for a successful process outcome. High energy ions in a broad IED are responsible for surface damage that may lead to device failure.[7,8] Eriguchi *et al.* reported the effect of plasma induced Si recess on device performance degradation.[9] Wang and Wendt[10] and Agarwal and Kushner[11] discussed ways of improving the selectivity of etching SiO$_2$ over Si using a narrow IED. Selectivity may be achieved by using a nearly monoenergetic IED, with the ion energy placed between the threshold for etching one material versus the other. For example, atomic layer etching of Si may be achieved with an ion energy between the thresholds for chemical sputtering (Si with a chemisorbed Cl layer) and physical sputtering (clean surface).[12]

Attainment of a narrow IED using a pulsed Ar plasma and synchronous dc bias on a "boundary electrode," during a specified time window in the afterglow, was reported previously.[13] Factors affecting the width of the distribution were

discussed. In this work, the effect of different noble gases (Kr and Xe, in addition to Ar) on the width of the IED was investigated. In addition, a method of maintaining an almost constant plasma density during the afterglow is presented.

II. EXPERIMENT

Figure 1 shows a schematic of the experimental apparatus; a detailed description was provided in Ref. 13. In brief, the inductively coupled plasma reactor was equipped with a Faraday shield to block capacitive coupling, and a boundary electrode that could be biased by a separate power supply. The plasma was pulsed by full amplitude modulation of 13.56 MHz power at a frequency of 10 kHz, with a duty cycle of 20%. The time-averaged net power was either 75 or 110 W. For ion energy analysis, a +23.2 V synchronous dc bias was applied to the boundary electrode, starting 25 μs after the onset of the afterglow, and continuing for the next 50 μs of the afterglow. This dc bias raised the plasma potential and caused positive ions to bombard a grounded substrate with an energy commensurate with the dc bias (assuming no collisions in the sheath). The inset in Fig. 1 shows a timing diagram of the pulsed plasma and the synchronous dc biasing of the boundary electrode.

A cylindrical Langmuir probe (Scientific Systems Smart-Probe^{TM}) sampled the plasma along the vertical axis of the cylindrical reactor. Time-resolved plasma parameters (electron temperature T_e, plasma potential V_p, electron density n_e, and ion density n_i) were measured by the Langmuir probe at the edge of the plasma (the same location as the IED measurements[13]), with no bias applied in the afterglow period. To measure the IED, the Langmuir probe was replaced with a home-built retarding field energy analyzer (RFEA).[14–16] The RFEA was surrounded with a metal ring (2 in. o.d. and 1 in. i.d.) flush with the top surface of the RFEA, to act as a guard ring and to better confine the plasma. The RFEA was made of a stack of three nickel grids and a stainless steel current collector plate, spaced 3 mm apart. The top grid was attached to
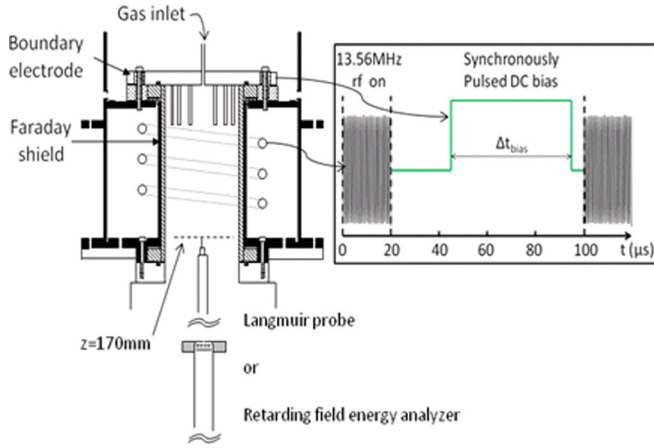
FIG. 1. (Color online) Schematic of the experimental system. The boundary electrode is located at the top of the cylindrical plasma reactor. A dc bias was applied synchronously to the boundary electrode during a specified time window in the afterglow of a pulsed discharge. The inset shows the timing of such a synchronous dc bias with respect to plasma pulsing. In this case, the dc bias was applied 25 μs after the start of the afterglow and it was kept on for 50 μs.

a grounded SS plate with a 0.3 mm pinhole in contact with the plasma. This grid prevented the plasma sheath from molding over the pinhole. The middle grid was biased with -30 V to repel electrons from the plasma, while the bottom grid was biased with a sawtooth ramp voltage and served as an energy discriminator to measure the ion energy distribution. The $I–V$ characteristic was measured using a LABVIEW program and differentiated to obtain the IED. The energy resolution of the RFEA was estimated using the formulas of Sakai and Katsumata[17] to be $\Delta E/E = 2\%$. The recorded IEDs were time averages over the pulse cycle. To improve the signal-to-noise ratio, 5000 sweeps were averaged for every IED. More details about the diagnostics can also be found in Ref. 13. Pulsed plasmas of Ar, Kr, or Xe gas (high purity, 99.999%) were operated at a chamber pressure of 14 mTorr and a gas flow rate of 40 sccm.

III. MODELING

A. Spatially average (global) model

The time-dependent electron temperature in the afterglow of a pulsed electropositive discharge was predicted based on a spatially average (global) model[18,19] of a cylindrical plasma with radius R and length L. This model assumes a uniform plasma density (and electron temperature) in the bulk, dropping off sharply at the sheath edge.

The time-dependent T_e was obtained from[20]

$$\frac{1}{T_e}\frac{dT_e}{dt} = \frac{P_{abs}}{W_e} - \left(\frac{2}{3}\frac{\varepsilon_c}{T_e} + 1\right)v_{iz}$$
$$- \left(\frac{2}{3}\frac{V_s + \frac{5}{2}T_e}{T_e} - 1\right)v_{loss}, \quad (1)$$

where $v_{iz} = K_{iz}n_g$ is the ionization frequency (K_{iz} is the ionization reaction rate coefficient and n_g is the neutral gas density), P_{abs} is the absorbed power, W_e is the plasma energy ($1.5en_eT_eV$), V_s is the sheath potential, ε_c is the collisional

energy loss per electron–ion pair created in the discharge, and $v_{loss} = u_B/L_{eff}$ is the charged particle loss frequency. u_B is the Bohm velocity and L_{eff} is the plasma characteristic length,

$$L_{eff} = \frac{V}{2\pi R^2 h_L + 2\pi R L h_R}. \quad (2)$$

Here V is plasma volume and h_L (h_R) is the ratio of plasma density at the axial (radial) sheath edge to that in the bulk plasma. In the afterglow, P_{abs} is zero and, since v_{iz} depends exponentially on T_e, the second term on the right-hand side of Eq. (1) can be neglected as T_e plummets a very short time into the afterglow. The equation for the time-dependent T_e can then be simplified as

$$\frac{1}{T_e}\frac{dT_e}{dt} = -\left(\frac{2}{3}\frac{V_s + \frac{5}{2}T_e}{T_e} - 1\right)v_{loss}(t), \quad (3)$$

which can be solved analytically to yield the time-dependent decay of $T_e(t)$ in the afterglow,[20]

$$T_e(t) = T_{e0}\left[1 + \frac{\left(\frac{2}{3}\frac{V_s + \frac{5}{2}T_e}{T_e} - 1\right)}{2}v_0 t\right]^{-2}, \quad (4)$$

where T_{e0} is the known (measured) temperature at the end of the active glow [i.e., beginning of the afterglow ($t = 0$)] and $v_0 = \left(\frac{eT_{e0}}{M}\right)^{\frac{1}{2}}/L_{eff}$. Since $\frac{1}{2}\left(\frac{2}{3}\frac{V_s + \frac{5}{2}T_e}{T_e} - 1\right) \approx 2$ for Ar, Kr, Xe, Eq. (4) can be simplified as

$$T_e(t) = T_{e0}[1 + 2v_0 t]^{-2}. \quad (5)$$

B. Spatially resolved fluid model

The Ar plasma density evolution in the afterglow was simulated using a simple two-dimensional diffusion model at the same conditions as in the experimental setup. The continuity equation for plasma density is given by

$$\frac{\partial n}{\partial t} = \nabla \cdot (D_a \nabla n), \quad (6)$$

where $D_a = D_i(1 + T_e/T_i)$ is the ambipolar diffusivity, and D_i is the ion diffusivity. Electroneutrality ($n_i = n_e = n$) was assumed. Reactions producing electrons are quenched very early in the afterglow; therefore, there is no source term in Eq. (6). The boundary conditions were $\Gamma = 0$ on the symmetry axis/plane, where Γ is the species flux, and $n \approx 0$ on the walls. The initial density profile was taken to be a cosine distribution in the axial direction and a Bessel function in the radial direction. The plasma density was computed during the afterglow as a function of time and position.

IV. RESULTS AND DISCUSSION

A. Time evolution of electron temperature

Time-resolved electron temperatures measured with the Langmuir probe are presented in Fig. 2. The application of
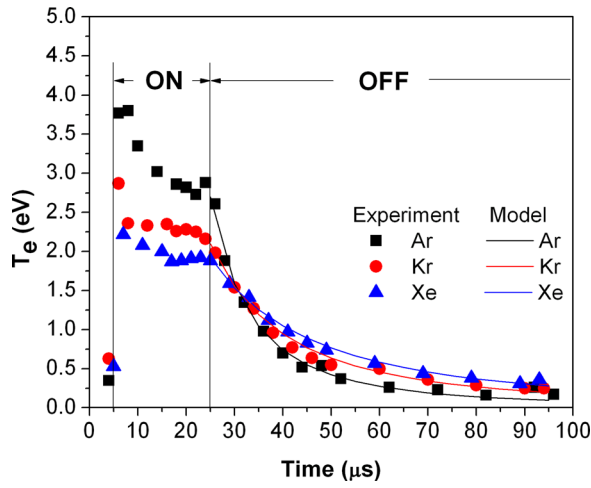
FIG. 2. (Color online) Time-resolved T_e measured by a Langmuir probe at the location of the RFEA in pulsed plasmas with different noble gases. Pressure and time-averaged power were the same for all cases (14 mTorr and 110 W, respectively). No dc bias was applied. The solid lines are global model predictions.

plasma power began at ~5 μs and ended at 25 μs. There was no bias applied during these measurements. T_e in the quasi-steady-state active glow is ordered as T_e (Ar) $> T_e$ (Kr) $> T_e$ (Xe). This is because the ionization potential is largest in Ar (more difficult to ionize the gas), while the electron diffusivity is smallest in Xe (smallest wall losses). However, the T_e hierarchy reverses a short time into the afterglow: T_e (Ar) $< T_e$ (Kr) $< T_e$ (Xe). During the afterglow, electron-impact reactions having an appreciable threshold are rapidly quenched, and volumetric losses of electron energy are negligible compared to the loss of electrons by diffusion to the walls. Electrons in the tail of the electron energy distribution function are lost first, cooling the distribution.[21,22] The electron diffusivity is highest for Ar and lowest for Xe, resulting in the observed hierarchy of electron temperatures.

This is also borne out by the global model of the discharge described earlier. The time evolution of the electron temperature in the afterglow of Ar, Kr, and Xe plasmas was predicted by using Eq. (5). The pressure was 14 mTorr and the gas temperature was taken to be 600 K. The reactor dimensions were $L = 7$ cm and $R = 4.3$ cm. The ion–neutral collision cross sections for Kr and Xe ($\sigma_{Kr} = 15.7 \times 10^{-15}$ cm^2 and $\sigma_{Xe} = 19.2 \times 10^{-15}$ cm^2) were taken from Ref. 23. For Ar, the average value ($\sigma_{Ar} = 10.2 \times 10^{-15}$ cm^2) from Refs. 19 and 23 was used. Equation (2) then yields $L_{eff} = 6.84$ cm for Ar, 7.64 cm for Kr, and 8.37 cm for Xe plasma. Using the measured electron temperatures at the end of the active glow for T_{e0} values, the predictions of the global model (Fig. 2, solid lines) capture the measured evolution of electron temperature in the afterglow very well.

B. Time evolution of electron and ion density

Measured time-resolved electron and ion densities are presented in Fig. 3. Plasma power was switched on at ~5 μs and off at 25 μs. Contrary to expectations, there is at most only a slight decay of either n_e or n_i in the 80 μs afterglow.

This was attributed to transport of electrons from the higher density central region of the plasma to the edge region, balancing the loss of plasma due to diffusion from the edge. Previous measurements in continuous wave plasmas, under otherwise the same conditions, showed four times higher plasma density at the center of the plasma compared to the edge, implying a strong density gradient.

The above-described 2D diffusion model was used to predict the time evolution of plasma density in the afterglow. The predicted density evolution at the location of the Langmuir probe is shown in Fig. 4, along with experimental data. The agreement between the model predictions and the experimental data is very good, considering the uncertainty in the data, especially late in the afterglow. This confirms that the nearly constant density is due to diffusion from the high charge density central part of the plasma, compensating the losses of plasma from the edge, where measurements were taken. The plasma density was predicted to decay rather rapidly at the center of the reactor (60 mm above of Langmuir probe position). At that location, the density dropped from 4 to 1×10^{11} cm^{-3} during the 80 μs duration of the afterglow. Subramonium and Kushner[24] showed similar simulation results in the Gaseous Electronics Conference reference cell. The plasma density decayed much slower in the plasma edge region compared to that at the center of the plasma. Maintaining a nearly constant
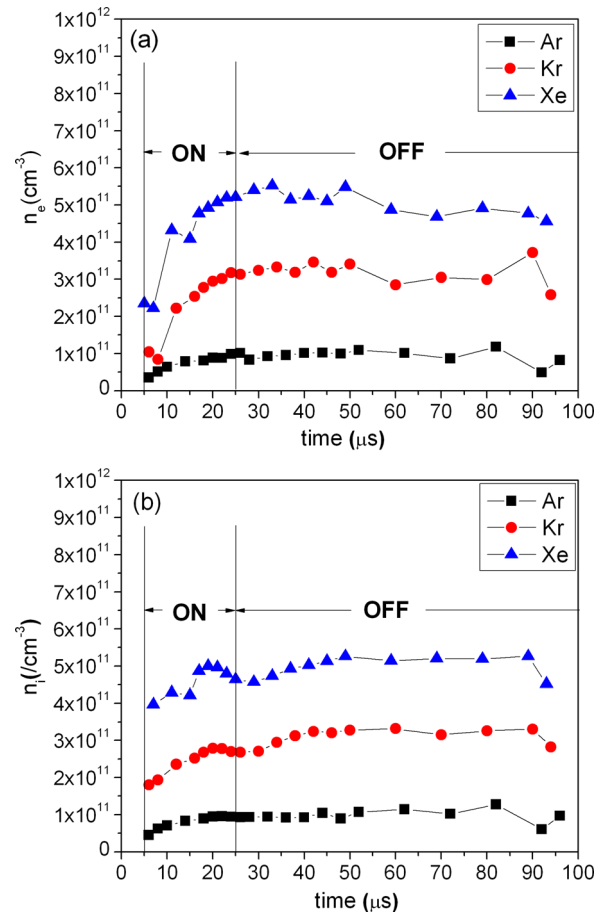

FIG. 3. (Color online) Time-resolved n_i (a) and n_e (b) measured by a Langmuir probe at the location of the RFEA in pulsed plasmas with different gases. The pressure was 14 mTorr and the time-averaged power was 110 W.
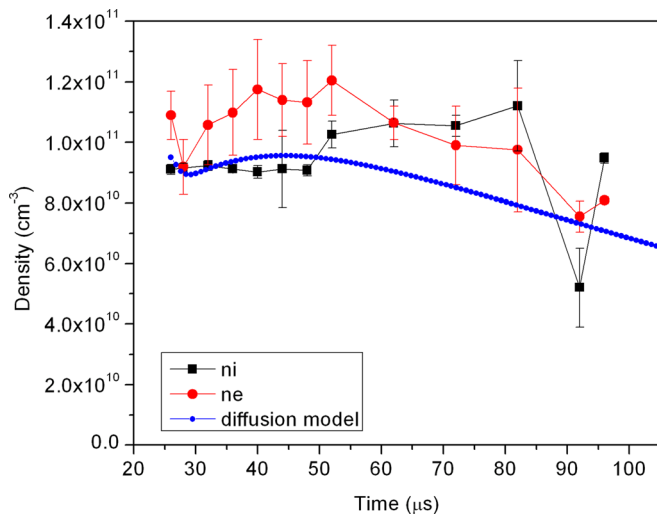
FIG. 4. (Color online) Time-resolved n_i and n_e for pulsed Ar plasma at 14 mTorr and 110 W during the afterglow. Experimental data are from Fig. 3. Thick line is the prediction of a 2D fluid simulation of the afterglow.

plasma density, even in a relatively long afterglow window (80 μs in the present case), can be advantageous for advanced etching processes using pulsed plasmas.

C. Ion energy distributions

Figure 5(a) shows the IED for each of the three gases. The broad lower-energy peak is due to ions during the active
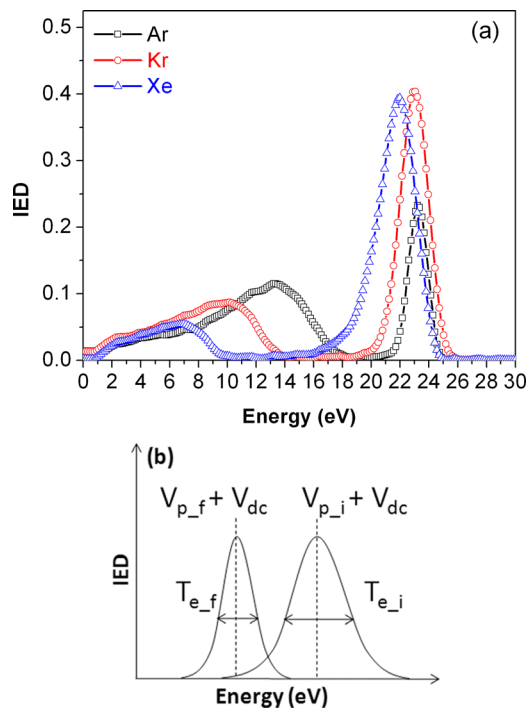

FIG. 5. (Color online) (a) IEDs measured by a retarding field energy analyzer (RFEA) in pulsed Ar, Kr, or Xe plasmas at 10 kHz plasma power modulation, with a duty cycle of 20%, and a time-averaged net power of 75 W. The boundary electrode was synchronously biased with +23.2 V dc from 25 to 75 μs after the start of the afterglow. Gas pressure = 14 mTorr. (b) Qualitative IEDs showing broadening mechanisms in pulsed plasmas. T_{e_i} and T_{e_f} are the initial and the final electron temperatures during the bias application window, respectively. V_{p_i} and V_{p_f} are the corresponding plasma potentials.

glow and portions of the afterglow when no bias is applied. The narrow higher-energy peak corresponds to ions extracted during the 50 μs of boundary electrode biasing in the afterglow.[13] The maximum value of the broad peak is a measure of the active glow plasma potential [$\sim$7, 10, and 13 V for Xe, Kr, and Ar, respectively, in Fig. 5(a)]. The area under the peak is proportional to the ion flux and, for comparable electron temperatures, ion density. Therefore, plasma density was ordered as Xe > Kr > Ar. This can be explained by the faster ionization rate and slower diffusion rate for Xe versus Kr versus Ar.

Figure 5(a) shows that the full width at half maximum (FWHM) of the narrow peaks are 1.6, 2.4, and 3.0 eV for Ar, Kr, and Xe, respectively. Several factors contribute to the IEDs of the different noble gases. The width of the IED at the sheath edge scales with T_e,[15,25] due to collisions in the presheath. Hence, higher T_e will yield a wider IED, as shown in Fig. 5(a). T_e in the afterglow is highest for Xe and lowest for Ar plasmas (see previous discussion), consistent with the ordering of the IED widths. After being accelerated in a collisionless sheath, the IED is shifted by the sheath potential (V_s) maintaining the original FWHM. (The sheath is essentially collisionless since the ion mean free path for Ar at 14 mTorr and 600 K is 7 mm, much longer than the sheath thickness of $\sim$0.2 mm, estimated using the Child law.) V_s decreases somewhat during the biasing period in the afterglow because of a decrease in the plasma potential. Figure 5(b) shows qualitative IEDs at the beginning and the end of the biasing window. The IED shifts to lower energies and becomes sharper with time. The measured IED in the afterglow is therefore a time-averaged distribution during the bias pulse, with a width comparable to the difference, ΔV_p, between plasma potentials at the beginning and end of biasing, $\Delta V_p = V_{p\_i} - V_{p\_f}$. $\Delta V_p = 2.6, 2.2$, and 1.8 V for Xe, Kr, and Ar, respectively, consistent with the ordering of the IED widths. Therefore, the combination of changes in T_e and V_p explains the magnitudes and ordering of the IED widths during biasing in the afterglow period.

The areas under the curves of the high energy and low energy peaks of the IEDs in Fig. 5(a) correspond to ion currents during the application of dc bias in the afterglow, and the remainder of the cycle (active glow plus afterglow without bias), respectively. Knowing the total open area (i.e., filtering ratio) of the RFEA grids, one can estimate ion densities from the measured currents and the electron temperature provided by Langmuir probe measurements. The ion densities calculated from the IEDs during the afterglow with bias, n_{i_IED}, were 1.9, 5.8, and $9.0 \times 10^{11}/\text{cm}^3$ for Ar, Kr, and Xe, respectively. These are about twice the ion densities measured by the Langmuir probe under the same conditions. n_{i_LP} was 1.0, 3.0, and $5.0 \times 10^{11}/\text{cm}^3$ for Ar, Kr, and Xe, respectively. Considering the errors associated with measuring absolute ion densities with a Langmuir probe, and the uncertainty of estimating the open area of the analyzer grids, the discrepancy seems reasonable. During the remainder of the cycle, n_{i_LP} was found to be 0.75, 2.5, and $4.5 \times 10^{11}/\text{cm}^3$, whereas $n_{i\_IED} = 1.6, 1.9$, and $1.2 \times 10^{11}/\text{cm}^3$ for Ar, Kr, and Xe, respectively. The larger

difference between the current densities estimated by the two methods for the period of no applied dc bias was attributed mainly to a falloff in the detection efficiency of the RFEA for low energy ions. Ions could be increasingly lost at the second grid (negatively biased to repel electrons) and/or not collected because the wider angular spread of low energy ions prevents some of them from passing through the 0.3 mm diam, 0.5 mm thick input aperture on the front of the RFEA. The increasing discrepancy between n_{i_IED} and n_{i_LP} is consistent with the shift of the active glow IED to lower energy for Xe versus Kr versus Ar, and is also in line with the much higher ion densities at low energies predicted by recent modeling studies of this reactor.[26]

V. SUMMARY AND CONCLUSIONS

IEDs were measured near the edge of pulsed inductively coupled plasmas in Ar, Kr, or Xe gas, while applying a synchronous dc bias, on a boundary electrode, during a specified time window in the afterglow. The IED in Ar was narrower than that in Kr, which in turn was narrower than the IED for Xe. This ordering was explained by the time-dependent behavior of the electron temperature and plasma potential for the three gases. Within a very short time after the beginning of the afterglow, the ordering of the electron temperatures was T_e (Xe) > T_e (Kr) > T_e (Ar), consistent with the ordering of the widths of the IED in the different noble gases, which scale with T_e because of collisions in the presheath. V_p also decreases with time during the application of bias in the afterglow, causing an additional broadening of the IED, due to a drift in the sheath potential. The measured electron temperature decay in the afterglow was accurately predicted by a global model.

The electron and ion density evolution in the afterglow was also measured near the plasma edge using a Langmuir probe. The plasma density was nearly constant, even over a long afterglow duration of 80 μs. This was attributed to transport of charge from the higher density central region of the plasma to the edge region, balancing the loss rate of plasma due to diffusion. A simple 2D ambipolar diffusion model was successful in predicting this trend. Maintaining this nearly constant plasma density during the afterglow may be beneficial in processes employing pulsed plasmas.

[1]R. T. C. Tsui, Phys. Rev. **168**, 107 (1968).
[2]P. Benoit-Cattin and L. C. Bernard, J. Appl. Phys. **39**, 5723 (1968).
[3]E. Kawamura, V. Vahedi, M. A. Lieberman, and C. K. Birdsall,. Plasma Sources Sci. Technol. **8**, R45 (1999).
[4]E. A. Edelberg and E. S. Aydil, J. Appl. Phys. **86**, 4799 (1999).
[5]T. Panagopoulos and D. J. Economou, J. Appl. Phys. **85**, 3435 (1999).
[6]S.-B. Wang and A. E. Wendt, J. Appl. Phys. **88**, 643 (2000).
[7]N. Yabumoto, M. Oshima, O. Michikami, and S. Yoshi, Jpn. J. Appl. Phys. **20**, 893(1981).
[8]T. Ohchi, S. Kobayashi, M. Fukasawa, K. Kugimiya, and T. Kinoshita,. Jpn. J. Appl. Phys. **47**, 5324 (2008).
[9]K. Eriguchi, A. Matsuda, Y. Nakakubo, M. Kamei, H. Ohta, and K. Ono, IEEE Electron Device Lett. **30**, 712 (2009).
[10]S.-B. Wang and A. E. Wendt, J. Vac. Sci. Technol. A **19**, 2425 (2001).
[11]A. Agarwal and M. J. Kushner, J. Vac. Sci. Technol. A **23**, 1440 (2005).
[12]T. Meguro, M. Hamagaki, S. Modaressi, T. Hara, Y. Aoyagi, M. Ishii, and Y. Yamamoto, Appl. Phys. Lett. **56**, 1552 (1990).
[13]H. Shin, W. Zhu, L. Xu, V. M. Donnelly, and D. J. Economou,. Plasma Sources Sci. Technol. **20**, 55001 (2011).
[14]D. Gahan, B. Dolinaj, and M. B. Hopkins, Rev. Sci. Instrum. **79**, 033502 (2008).
[15]U. Kortshagen and M. Zethoff,. Plasma Sources Sci. Technol. **4**, 541 (1995).
[16]J. R. Woodworth, M. E. Riley, D. C. Meister, B. P. Aragon, M. S. Le, and H. H. Sawin, J. Appl. Phys. **80**, 1304 (1996).
[17]Y. Sakai and I. Katsumata, Jpn. J. Appl. Phys., Part 1 **24**, 337 (1985).
[18]M. V. Malyshev, V. M. Donnelly, J. I. Colonell, and S. Samukawa, J. Appl. Phys. **86**, 4813 (1999).
[19]M. A. Lieberman and A. J. Lichtenberg, *Principles of Plasma Discharges and Materials Processing*, 2nd ed. (Wiley, New York, 1995)
[20]M. A. Lieberman and S. Ashida, Plasma Sources Sci. Technol. **5**, 145 (1996).
[21]M. A. Biondi, Phys. Rev. **93**, 1136 (1954).
[22]S. Gorchakov, D. Loffhagen, and D. Uhrlandt, Phys. Rev. E **74**, 066401 (2006).
[23]R. N. Varney, Phys. Rev. **88**, 362 (1952).
[24]P. Subramonium and M. J. Kushner, J. Vac. Sci. Technol. A **20**, 313 (2002).
[25]K.-U. Riemann, Phys. Fluids **24**, 2163 (1981).
[26]M. Logue, H. Shin, W. Zhu, L. Xu, V. M. Donnelly, D. J. Economou, and M. J. Kushner, "Ion energy distributions in pulsed inductively-coupled plasmas having a pulsed boundary electrode," *64th Gaseous Electronics Conference*, Salt Lake City, UT, BAPS.2011.GEC.LW3.6 (2011).